Monthly Notices
of the
ROYAL ASTRONOMICAL SOCIETY

MNRAS **460,** 1898–1911 (2016)
Advance Access publication 2016 May 12

doi:10.1093/mnras/stw1119

Detecting edges in the X-ray surface brightness of galaxy clusters

J. S. Sanders,[1]★ A. C. Fabian,[2] H. R. Russell,[2] S. A. Walker[2] and K. M. Blundell[3]

[1]*Max-Planck-Institut für extraterrestrische Physik, Giessenbachstrasse 1, D-85748 Garching, Germany*
[2]*Institute of Astronomy, Madingley Road, Cambridge CB3 0FT, UK*
[3]*University of Oxford, Astrophysics, Keble Road, Oxford OX1 3RH, UK*

Accepted 2016 May 10. Received 2016 May 10; in original form 2016 January 14

ABSTRACT

The effects of many physical processes in the intracluster medium of galaxy clusters imprint themselves in X-ray surface brightness images. It is therefore important to choose optimal methods for extracting information from and enhancing the interpretability of such images. We describe in detail a gradient filtering edge detection method that we previously applied to images of the Centaurus cluster of galaxies. The Gaussian gradient filter measures the gradient in the surface brightness distribution on particular spatial scales. We apply this filter on different scales to *Chandra X-ray observatory* images of two clusters with active galactic nucleus feedback, the Perseus cluster and M 87, and a merging system, A 3667. By combining filtered images on different scales using radial filters spectacular images of the edges in a cluster are produced. We describe how to assess the significance of features in filtered images. We find the gradient filtering technique to have significant advantages for detecting many kinds of features compared to other analysis techniques, such as unsharp masking. Filtering cluster images in this way in a hard energy band allows shocks to be detected.

Key words: techniques: image processing – X-rays: galaxies: clusters.

1 INTRODUCTION

X-ray emission from clusters is mainly due to bremsstrahlung emission (Felten et al. 1966; Mitchell et al. 1976) from the hot intracluster medium (ICM). The X-ray flux is proportional to the square of density, with some temperature dependence, and so is a sensitive tracer of variations in the thermodynamic properties of the ICM.

Although relaxed clusters are largely hot atmospheres in hydrostatic pressure equilibrium, density and temperature variations are important probes of astrophysical processes within the cluster and of cluster-wide perturbations such as mergers. Active galactic nucleus (AGN) feedback in clusters (Fabian 2012) injects bubbles of radio plasma into the ICM, displacing the X-ray emitting gas and creating cavities in X-ray images (e.g. Böhringer et al. 1993; Fabian et al. 2000; McNamara et al. 2000). In addition, AGN are observed to shock their surroundings (e.g. Forman et al. 2007; Randall et al. 2015) and likely generate sound waves in the ICM (Fabian et al. 2006; Sanders & Fabian 2008; Blanton et al. 2011). These processes are seen in simulations of AGN feedback (e.g. Ruszkowski et al. 2004; Sijacki & Springel 2006).

Cold fronts – discontinuities in temperature and density – are extremely common in clusters (Markevitch & Vikhlinin 2007). These are seen in both merging (e.g. Vikhlinin, Markevitch & Murray 2001) and relaxed (e.g. Paterno-Mahler et al. 2013) clusters. In the relaxed cases, the fronts are believed to be caused by gas sloshing in the potential well due to the passage of a subcluster (Ascasibar & Markevitch 2006). Such sloshing may remain for several Gyr and can give rise to several edges within a single cluster. Merging subclusters additionally generate shocks, also seen as surface brightness edges (e.g. Markevitch et al. 2002; Russell et al. 2010).

Mergers and AGN feedback can inject turbulence in the ICM (Norman & Bryan 1999). Turbulence within the ICM should be associated with gas density and therefore surface brightness variations which can be quantified (Churazov et al. 2012; Sanders & Fabian 2012; Zhuravleva et al. 2014; Walker, Sanders & Fabian 2015).

The radial variation in density in clusters, particularly in relaxed objects, gives rise to steeply peaked surface brightness profiles. Therefore, it is often difficult to see variations in surface brightness profile on these mountainous X-ray peaks. Various techniques have been developed to enhance the structure seen in images of galaxy clusters, allowing variations to be observed. These include dividing or subtracting a symmetric model, such as the β model (e.g. Arnaud et al. 2001), or the average at each radius (e.g. Churazov et al. 1999). More complex models can also be used, such as fits to surface brightness contours with ellipses (Sanders & Fabian 2012).

Another common technique is to use unsharp masking of cluster images to highlight smaller scale substructure (e.g. Fabian et al. 2003a). The typical method is to smooth the image first by a Gaussian with a large width and subtract (or divide) this from the same image smoothed by a Gaussian with a smaller width. The process results in an image which suppresses both large- and small-scale structure. A further method to suppress unwanted cluster signal is a Fourier bandpass filter (Sanders & Fabian 2008). However, a

★ E-mail: jsanders@mpe.mpg.de

risk with Fourier techniques is that spurious circular ringing artefacts from edges and point sources can be introduced if frequency cut-offs in the applied filter are too sharp.

Here, we apply a gradient measuring filter to X-ray images of galaxy clusters. Finding edges and measuring gradients in surface brightness are useful, because all the astrophysical processes we have previously mentioned introduce density variations, and therefore surface brightness gradients, into X-ray images. For example, shocks and cold fronts produce edges (i.e. very steep gradients), while sound waves should produce alternating flat and steep gradients. As we are not interested in the total X-ray emission in a region, using the gradient removes much of the X-ray peak. Gradient filtering has previously been used in examining simulations of galaxy clusters to look for edges associated with cold fronts and sloshing (Roediger et al. 2013).

The use of the Gaussian gradient magnitude (GGM) filter was introduced to X-ray analysis in our study of deep *Chandra* observations of the Centaurus cluster (Sanders et al. 2016). The GGM filter calculates the gradient of an image assuming Gaussian derivatives (with a width σ). In comparison, the Sobel operator, a type of gradient filter, convolves two 3×3 matrices with the image and can be used to compute the magnitude of the gradient in an image on a pixel-by-pixel basis. The advantage of the GGM filter over the Sobel filter is that σ can be adjusted to measure the gradient over more or fewer pixels depending on the data quality and the scale of the features of interest. In X-ray cluster images, a large σ would be used for regions in the outskirts where there are few or no X-ray counts per pixel and a small value in the centre where there are many counts.

In this work, we apply the GGM filter to other high-quality data sets from the *Chandra* archive to demonstrate that the technique is a powerful method for the identification of physical processes taking place in the ICM. We examine two relaxed clusters with short central cooling times and active AGN feedback and one disturbed system undergoing a merger. In the Perseus cluster, A 426, there are multiple X-ray cavities (Fabian et al. 2000; Böhringer et al. 2004), a weak shock (Fabian et al. 2003a), ripples (Fabian et al. 2006), which may be sound waves from AGN feedback and uplifted high metallicity material (Sanders, Fabian & Dunn 2005). M 87 contains a bright jet, multiple bubble-like cavities (Young, Wilson & Mundell 2002) and weak shocks (Forman et al. 2005, 2007). There are cool arms of metal-rich material being dragged out by the radio bubbles (Young et al. 2002; Simionescu et al. 2007; Million et al. 2010). A 3667 is a system undergoing a merger (Knopp, Henry & Briel 1996) and hosts a sharp surface brightness discontinuity, a cold front, indicating material is moving through the ambient gas with a Mach number of $\sim$1 (Vikhlinin et al. 2001). Optically, the cluster has two distinct sets of galaxies (Sodre et al. 1992) and a radio relic (Röttgering et al. 1997).

2 DATA PREPARATION

We downloaded the data sets listed in Tables 1, 2 and 3 from the *Chandra* archive. The data sets were reprocessed using CIAO (Fruscione et al. 2006) version 4.7 and CALDB version 4.4.10. We filtered bad time periods using X-ray light curves. For observations taken with ACIS-S (the S subarray on the Advanced CCD Imaging Spectrometer), we extracted light curves from CCD 5, if available, otherwise CCD 7. When analysing ACIS-I data, we used CCDs 0, 1 and 2. The bad time periods were chosen using an iterative σ clipping algorithm, clipping 200 s periods with rates outside 2.5σ, where σ is the Poisson error on the mean count rate. The individual observations were reprojected to the coordinate system of the marked reference observations, indicated with an asterisk (*) in Tables 1, 2 and 3. Images were constructed for each observation and CCD using single-detector pixel binning.

Table 1. *Chandra* data sets examined for the Perseus cluster. For each observation, we list the observation identifier, observation starting date, exposure (unfiltered and after filtering for flares in ks) and the ACIS CCDs from which the data were examined, with the ACIS mode (S or I). * marks the reference observations that others were reprojected to.

OBSID	Date	Exposure	Filtered	CCDs
502	1999-09-20	5.1	2.4	I: 0,1,2,3,6,7
503	1999-11-28	9.0	8.8	S: 2,3,6,7,8
1513	2000-01-29	24.9	10.5	S: 2,3,6,7,8
3209	2002-08-08	95.8	94.0	S: 1,3,6,7
4289	2002-08-10	95.4	93.0	S: 1,3,6,7
6139	2004-10-04	56.4	53.2	S: 2,3,5,6,7
4946	2004-10-06	23.7	23.3	S: 2,3,5,6,7
4948	2004-10-09	118.6	111.3	S: 2,3,5,6,7
4947	2004-10-11	29.8	29.4	S: 2,3,5,6,7
4949	2004-10-12	29.4	29.2	S: 2,3,5,6,7
4950	2004-10-12	96.9	75.6	S: 2,3,5,6,7
*4952	2004-10-14	164.2	147.3	S: 2,3,5,6,7
4951	2004-10-17	96.1	93.8	S: 2,3,5,6,7
4953	2004-10-18	30.1	29.7	S: 2,3,5,6,7
6145	2004-10-19	85.0	84.6	S: 2,3,5,6,7
6146	2004-10-20	47.1	42.4	S: 2,3,5,6,7
11716	2009-10-10	39.6	38.1	I: 0,1,2,3,6
12025	2009-11-25	17.9	11.7	I: 0,1,2,3,6,7
12033	2009-11-27	18.9	12.0	I: 0,1,2,3,6,7
11713	2009-11-29	112.2	75.9	I: 0,1,2,3,6,7
12036	2009-12-02	47.9	34.8	I: 0,1,2,3,6,7
11715	2009-12-02	73.4	68.6	I: 0,1,2,3,6
12037	2009-12-05	84.6	79.1	I: 0,1,2,3,6
11714	2009-12-07	92.0	80.1	I: 0,1,2,3,6
Total			1328.7	

Table 2. *Chandra* data sets examined for M 87. The columns are the same as for Table 1.

OBSID	Date	Exposure	Filtered	CCDs
352	2000-07-29	37.7	33.5	S: 2,3,6,7
3717	2002-07-05	20.6	10.5	S: 2,3,6,7
*2707	2002-07-06	98.7	88.2	S: 2,3,6,7
6186	2005-01-31	51.6	42.8	I: 0,1,2,3
5826	2005-03-03	126.8	120.0	I: 0,1,2,3
5827	2005-05-05	156.2	147.7	I: 0,1,2,3
7212	2005-11-14	65.2	61.2	I: 0,1,2,3
7210	2005-11-16	30.7	27.5	I: 0,1,2,3
7211	2005-11-16	16.6	15.7	I: 0,1,2,3
5828	2005-11-17	33.0	31.4	I: 0,1,2,3
15180	2013-08-01	138.8	137.2	I: 0,1,2,3
15178	2014-02-17	46.5	46.1	I: 0,1,2,3
16585	2014-02-19	45.0	44.0	I: 0,1,2,3
16586	2014-02-20	49.2	48.4	I: 0,1,2,3
16587	2014-02-22	37.3	37.0	I: 0,1,2,3
15179	2014-02-24	41.4	40.2	I: 0,1,2,3
16590	2014-02-27	37.6	37.0	I: 0,1,2,3
16591	2014-02-27	23.5	22.9	I: 0,1,2,3
16592	2014-03-01	35.6	35.0	I: 0,1,2,3
16593	2014-03-02	37.6	36.8	I: 0,1,2,3
Total			1063.2	

Table 3. *Chandra* data sets examined for A 3667. The columns are the same as for Table 1.

OBSID	Date	Exposure	Filtered	CCDs
513	1999-09-22	44.8	40.1	I: 0,1,2,3,5,6
889	2000-09-09	50.3	49.7	I: 0,1,2,3,6,7
*5751	2005-06-07	128.9	125.0	I: 0,1,2,3,6
6292	2005-06-10	46.7	45.7	I: 0,1,2,3,6
5752	2005-06-12	60.4	59.4	I: 0,1,2,3,6
6295	2005-06-15	49.5	48.9	I: 0,1,2,3,6
5753	2005-06-17	103.6	74.0	I: 0,1,2,3,6
6296	2005-06-19	49.4	48.6	I: 0,1,2,3,6
7686	2007-06-23	5.0	5.0	I: 0,1,2,3
Total			496.5	

Spatial masks were applied to the data to improve the quality of the output images. We excluded the outer edges of the ACIS-I array and those of individual ACIS-S CCDs. It is unclear why these steps should be necessary, but doing these removed structures associated with the edges. For M 87, we also applied narrow exclusion regions along the CCD read-out direction to remove the readout streak associated with out-of-time events. In the Perseus cluster, we masked out some regions which were far off-axis in some observations but covered by other observations with much better point spread functions. For example, we masked out the inner few arcmin in the offset ACIS-I observations, which were covered by on-axis ACIS-S observations.

We created exposure maps for each observation and CCD using MKEXPMAP. As input spectra for the exposure map calculation, we assumed for Perseus a 6 keV plasma, with a metallicity of $0.5\,Z_{\odot}$, absorption equivalent to a Hydrogen column of $10^{21}\,cm^{-2}$ and a redshift of 0.0183 (Sanders & Fabian 2007). For M 87, we assumed a temperature of 2.2 keV, a metallicity of $1.1\,Z_{\odot}$, absorption of $1.93 \times 10^{20}\,cm^{-2}$ (Million et al. 2010) and a redshift of 0.004 283 (Cappellari et al. 2011). For A 3667 we took the temperature to be 7 keV and the ICM abundance to be $0.3\,Z_{\odot}$ (Vikhlinin et al. 2001), we used redshift of 0.0556 (Struble & Rood 1999) and the Galactic column of $4.44 \times 10^{20}\,cm^{-2}$ (Kalberla et al. 2005).

Standard blank-sky background event files were used to remove the instrumental and diffuse X-ray background. For each foreground observation, we identified the appropriate backgrounds for each of the CCDs. We filtered out events which fell on bad pixels of the respective foreground observations. The exposure time of each background data set was adjusted to match the foreground rate in the 9 to 12 keV band. If the exposure times for the different CCD backgrounds were different, we reduced the exposure times to match the shortest background, discarding random events to keep the rate the same. The backgrounds for each CCD were then merged and reprojected to match the aspect of the respective foreground observations. We then adjusted these observation backgrounds to have the same ratio of exposure time to total background as the respective foreground observation had to the total foreground exposure, by reducing exposure times and discarding events appropriately. The observation backgrounds were reprojected to the reference foreground observation. Background images for each observation and CCD were made using the same binning as the foreground images.

Total exposure-corrected and background-subtracted images (Fig. 1, left-hand panels) were then calculated from the foreground, background and exposure-map images. First, the spatial masks were applied to each image. The total background image was then subtracted from the total foreground image after scaling by the ratio of exposure times. The total background-subtracted image was then divided by the total exposure map. We identified point sources in the image by eye (the usual WAVDETECT detection tool became confused by the high surface brightness central structures in Perseus and M 87). To cosmetically remove these from our exposure-corrected images, we replaced pixels inside the point source regions with random values selected from the immediately surrounding pixels. These cosmetically corrected images can be seen in Fig. 1 (right-hand panels).

3 GRADIENT FILTERING

3.1 Single scale filtering

The GGM filter calculates the gradient of the image assuming Gaussian derivatives. The gradient of the image is computed along the two axes by convolving the image by the gradient of a 1D Gaussian function. These two gradient images are combined to create a total gradient image. We used the implementation from SCIPY (http://scipy.org/). As inputs we used the unsmoothed exposure-corrected background-subtracted images, with the point sources cosmetically removed.

3.1.1 The Perseus cluster

Fig. 2 shows filtered images of the Perseus cluster using six exponentially increasing size scales. For each value of σ, we show different regions of the cluster as it becomes harder to measure gradients using small σ when the count rate becomes lower (see Section 3.2). Using $\sigma = 1$ and 2, the filtered image is sensitive to the finest structures in the centre, which include the edges of the inner cavities and the shocked region surrounding them (Fabian et al. 2006). Furthermore, some of the features associated with the absorbing high-velocity system and cool X-ray emitting filaments (Fabian et al. 2003b) are visible. Increasing the scales to 2 and 4, the cool spiral looping around the north of the cluster (Sanders et al. 2004) can be seen. To the north is the 'fountain', a structure seen in soft X-rays and by its H α emission (Fabian et al. 2006). In addition, the ripples in X-ray surface brightness can be seen to the eastern side of the cluster. In the 4 and 8 maps, the outer north-west and southern ghost cavities become visible, which are pointed to by low frequency radio spurs (Fabian et al. 2002). Further out, in the 8 and 16 maps, is the western edge (Churazov et al. 2003; Fabian et al. 2011), curving in the same direction as the inner spiral and at a radius of $\sim$110 kpc. The top of the curve is flattened and is associated with a surface brightness depression, one of a series in that direction (Sanders & Fabian 2007; Fabian et al. 2011). These features may be ancient relics of AGN activity, indicated by the radio emission and long H α filament pointing towards them. In the 8 and 16 maps to the south is the inverted-edge known as the 'bay', which may be another accumulation of previous AGN activity. On the largest scales, the core of the cluster appears to be contained within a 9 arcmin radius (200 kpc) egg-shaped region.

3.1.2 M 87

The X-ray-emitting jet in M 87 (Marshall et al. 2002; Wilson & Yang 2002) is clearly seen at the centre of the smallest scale map (Fig. 3). Surrounding the jet lies a cocoon of relativistic plasma which creates cavities in the X-ray emission in the jet and counter-jet directions (Young et al. 2002; Forman et al. 2007). In the $\sigma = 4$ map are the two well-known arms of soft X-ray emission

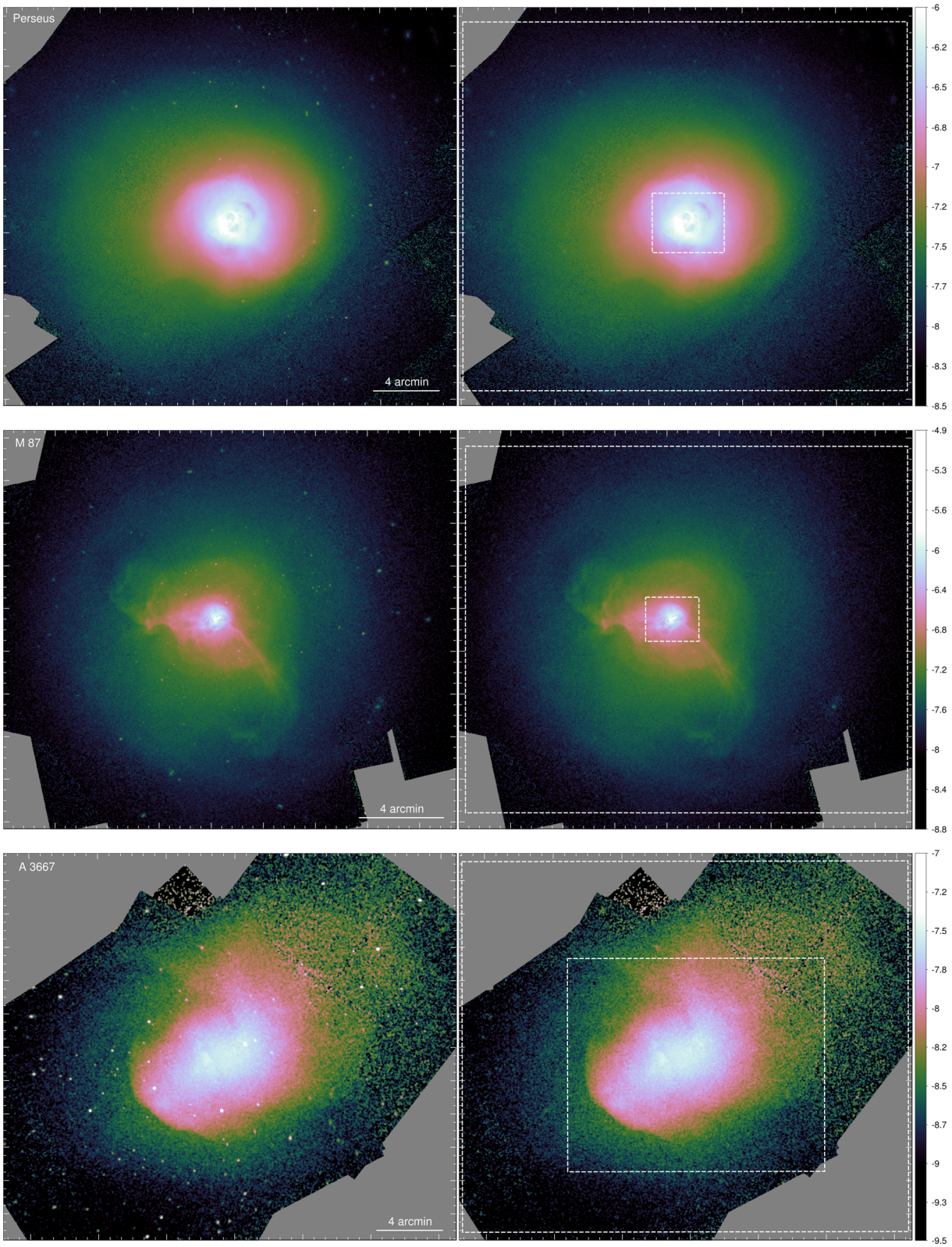

Figure 1. Exposure-corrected background-subtracted images of the Perseus cluster (top row), M 87 (centre row) and A 3667 (bottom row) in the 0.5 to 7 keV band. The left-hand panels include the point sources, while they are cosmetically hidden in the right-hand panels. The colour bar units are $\log_{10}$ photon cm^{-2} s^{-1} pixel^{-1}. The Perseus and M 87 images were smoothed by a Gaussian of 2 pixels (0.984 arcsec), while A 3667 was smoothed by 4 pixels. North is to the top and east is to the right in all the images in this paper. The white dashed boxes show the range in areas shown in the individual scale images.

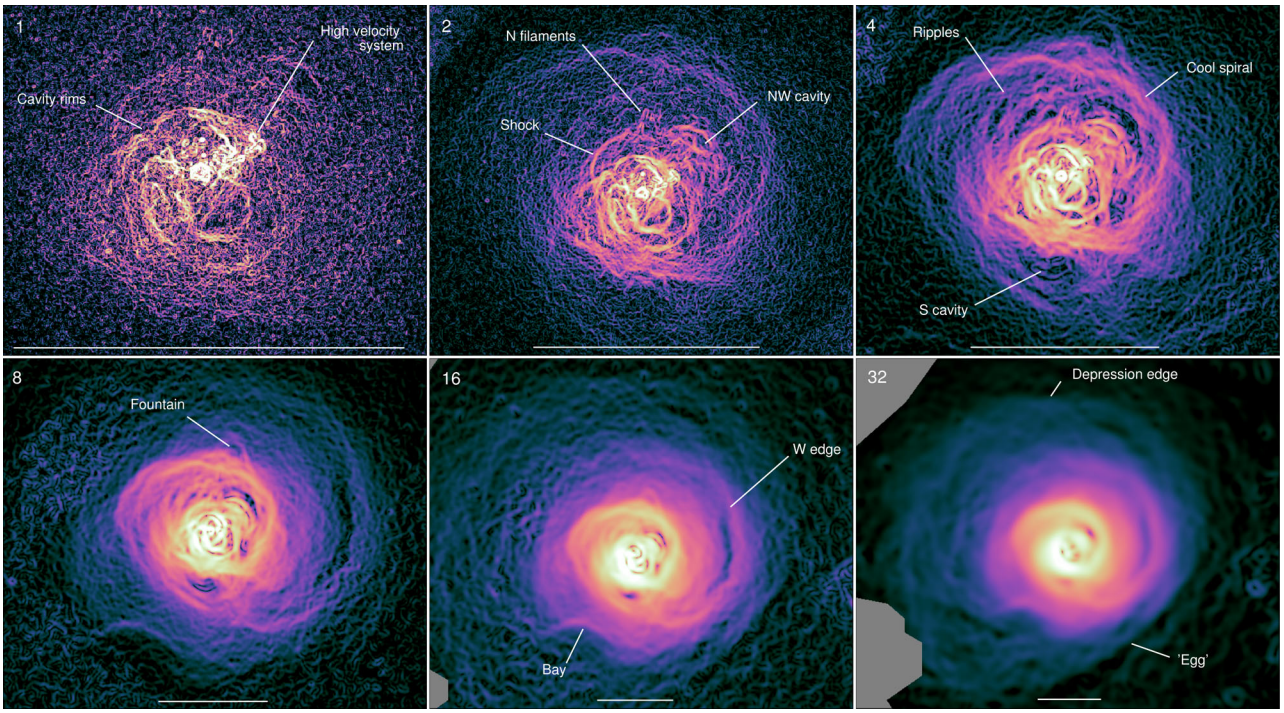

Figure 2. GGM-filtered images of the Perseus cluster with $\sigma = 1, 2, 4, 8, 16$ and 32 pixels (1 pixel is 0.492 arcsec). The bar has a length of 4 arcmin (89 kpc). The smallest and largest regions shown are indicated in Fig. 1.

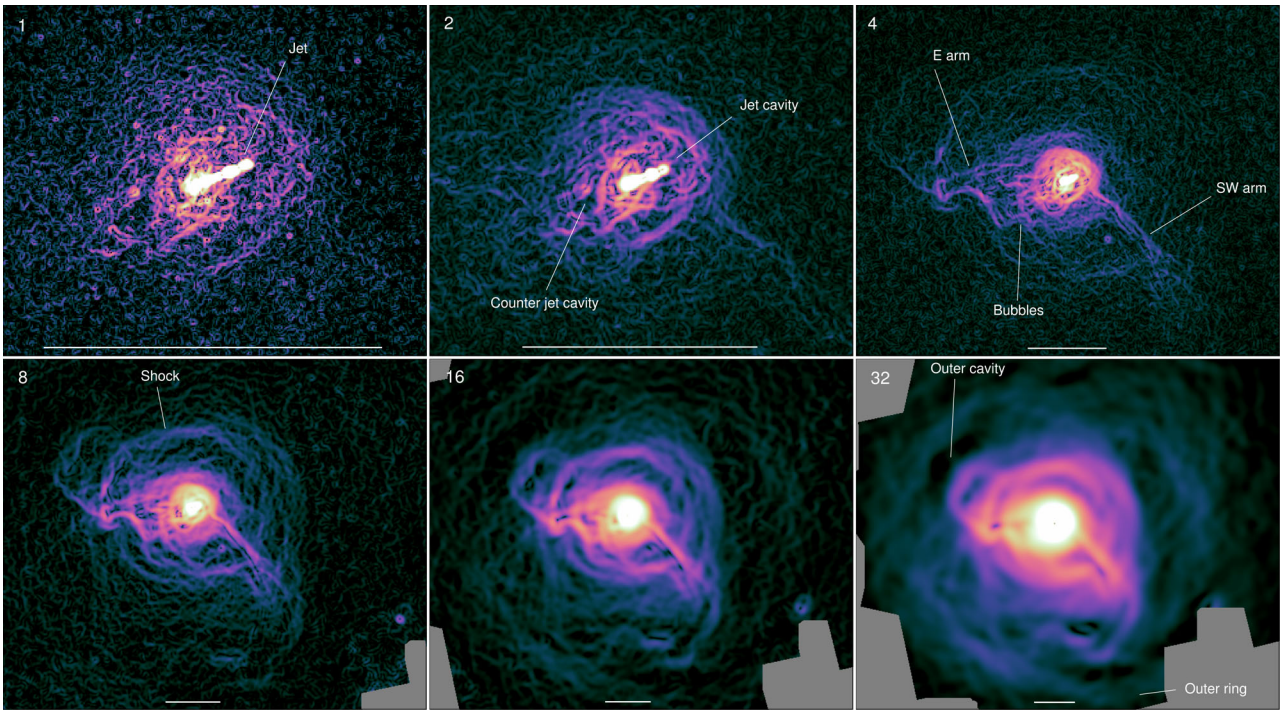

Figure 3. GGM-filtered images of M 87 with $\sigma = 1, 2, 4, 8, 16$ and 32 pixels (1 pixel is 0.492 arcsec). The bar has a length of 2 arcmin. Assuming a distance of 16.1 Mpc (Tonry et al. 2001), this corresponds to 9.4 kpc. The smallest and largest regions probed are shown in Fig. 1.

(Böhringer et al. 1995) extending out from the cluster along the arms of the radio source, likely metal-rich material lifted by the radio bubbles (Young et al. 2002; Simionescu et al. 2007; Million et al. 2010). The inner 10 kpc contains a series of bubbly structures, particularly along the eastern arm. The arm may be made up of a series of buoyant bubbles. In the eastern arm, the radio plasma and X-rays are cospatial, while along the south-western arm they are anticoincident (Forman et al. 2007) and appear to spiral around each other (Forman et al. 2005). Surrounding the nucleus with a radius of $\sim$13 kpc is a circular structure (Young et al. 2002; Forman et al. 2005), which is a weak shock (Forman et al. 2007). The $\sigma = 8$ pixel map shows that there are a series of edges which have

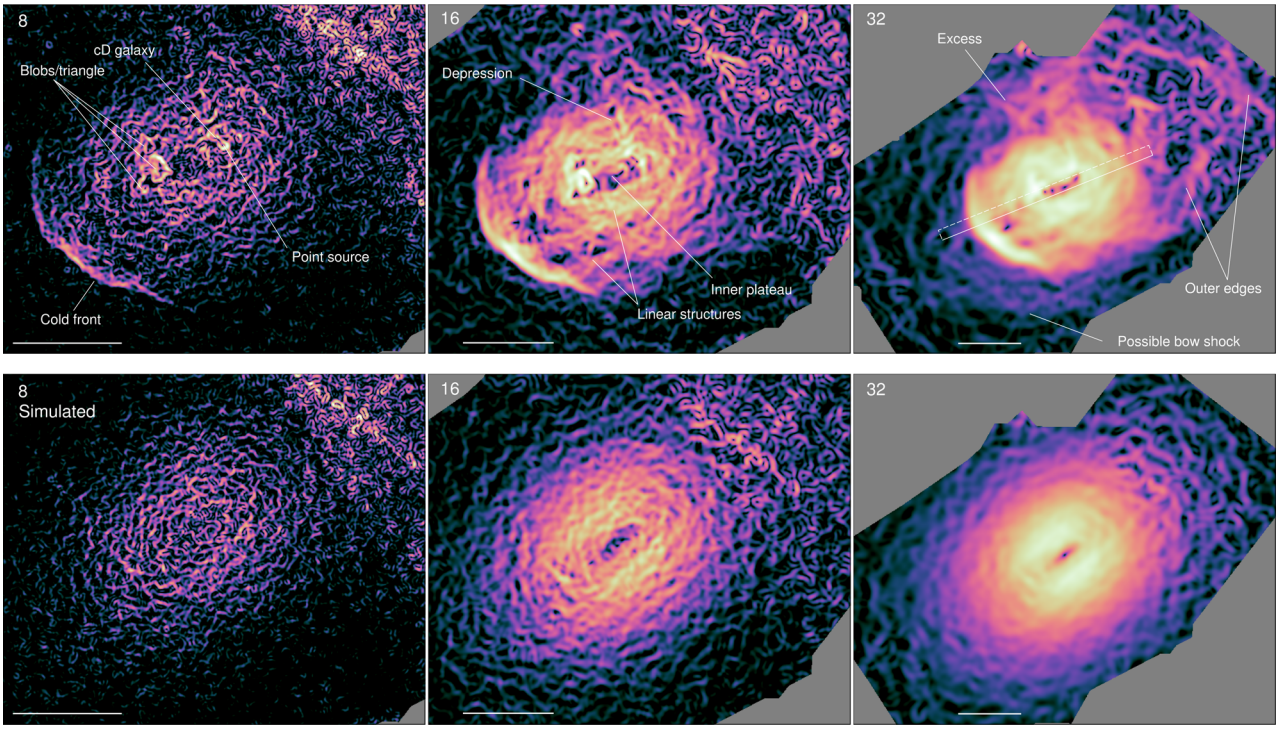

Figure 4. (Top row) GGM-filtered images of A 3667 with $\sigma = 8$, 16 and 32 pixels (1 pixel is 0.492 arcsec). The bar has a length of 4 arcmin (260 kpc). The smallest and largest regions here are shown in Fig. 1. The white box shows the region examined in the surface brightness and gradient profiles. (Bottom row) Filtered images of a Poisson realization of an elliptical β model fitted to the X-ray data, showing the large-scale gradient and noise.

a similar curvature to the shock, particularly in the region towards the south-west. There appears a second edge beyond the shock towards the north-east. We also see linear structures where the arms cross the shock. On the largest scales are outer cavities in the X-ray emission, surrounded by an other ring (Forman et al. 2007).

3.1.3 A 3667

There is less dynamic range in the image of A 3667 and so we only display the filtered maps for three spatial scales (Fig. 4 top row). Despite this, the filtering enhances a number of structures, many of which are not obvious in the original image. To help assess the significance of features, we show simulated images of the cluster in Fig. 4 (bottom row). These are based on an elliptical β model fit to the X-ray data, which has no structure except for a central core. A Poisson realization of the fit was filtered in the same way as the original data, showing the overall gradient and noise. To examine the significance of the features, we calculated profiles along the main axis of the cluster in surface brightness and GGM-filtered images on different scales (Fig. 5), including the $\sigma = 4$ scale. For comparison, we plot the profiles from the simulated model, which reproduces the overall gradient profiles and level of noise. There are edges seen in the data on all filtering scales which are not seen in the filtered model. There are significant sharp structures seen in the $\sigma = 4$ and 8 profiles which become washed out or mixed with other structures in the larger scale maps. On larger scales, the gradient filter reveals longer scale gradients which are easily missed in the noise in the smaller scale maps.

The most prominent structure is the well-known cold front indicating that the bright X-ray emitting region is moving through its surroundings at approximately sonic speeds (Vikhlinin et al. 2001). In these deeper data, we see that the edge is not perfectly smooth but there are features along it, likely Kelvin–Helmholtz instabilities. There is some faint X-ray emission associated with the cD galaxy, but a bright point source lies 20 arcsec (22 kpc) to the south-west. We were not able to fully remove this point source given its brightness, size and complex surrounding structure. To the south-east of the galaxy are bright well-defined blobs, clearly seen in the original X-ray image, one of which is a triangle-shaped region approximately 60 kpc in size. These regions are lower in temperature in their surroundings and have sharp edges. They appear to be in rough pressure equilibrium with their surroundings. They could be material stripped during the merger, but it is unclear where the material was stripped from.

Running between the central galaxy and the triangle is a relatively featureless region, labelled the inner plateau. Surrounding this plateau are many linear structures, in particular behind the cold front. These could be projected Kelvin–Helmholtz instabilities (see fig. 8 of Roediger et al. 2013). We see the edges of a large-scale excess and depression, claimed to be 300-kpc-long Kelvin–Helmholtz instabilities (Mazzotta, Fusco-Femiano & Vikhlinin 2002). At the north-west of our field, where the data quality is poorer, are long linear edges (labelled Outer Edges). These structures can also be seen in the deep *XMM* data of Finoguenov et al. (2010). They are not coincident with the edge of the radio relic to the north of the cluster, but lie a few hundred kpc inside them. They could mark the edge of a stripped tail of material, more easily seen in the *XMM* data. To the south of the cold front is another edge, likely the edge detected by Vikhlinin et al. (2001), which was identified by them as a possible bow shock.

3.2 Detecting gradients in Poisson noise images

The ability of the GGM filter to detect a gradient in surface brightness depends on the magnitude of the jump, the length it occurs

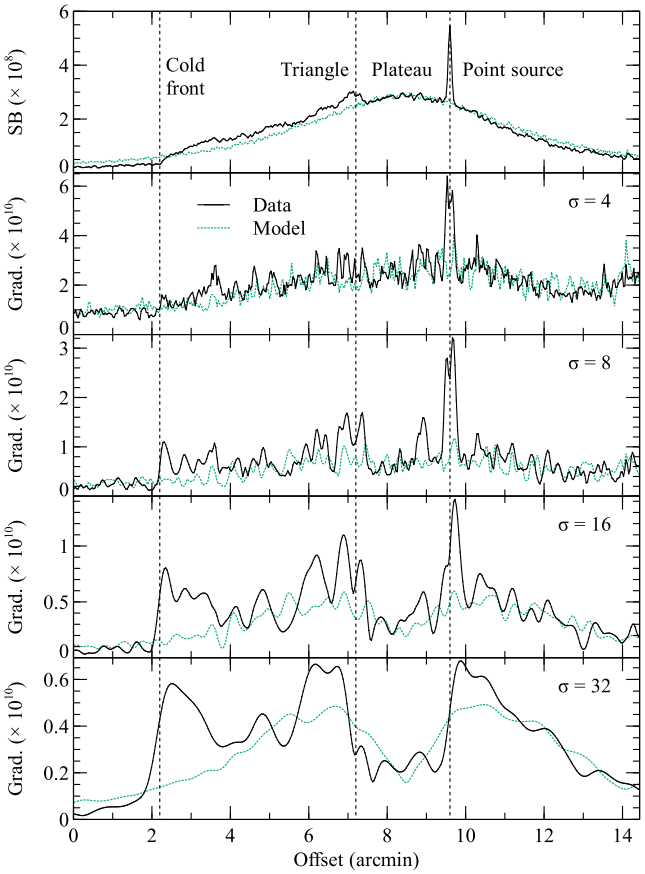

Figure 5. Surface brightness and gradient profiles in a strip across A 3667 from the south-west to the north-east (Fig. 4). The X-ray surface brightness in photon $\mathrm{cm}^{-2}\,\mathrm{s}^{-1}$ is shown in the top panel. The other panels show the gradient magnitude for the scales shown in photon $\mathrm{cm}^{-2}\,\mathrm{s}^{-1}$ pixel^{-1}, for 0.492 arcsec pixels. For comparison are plotted the surface brightness and filtered profiles of a Poisson realization of a model (Fig. 4 bottom row).

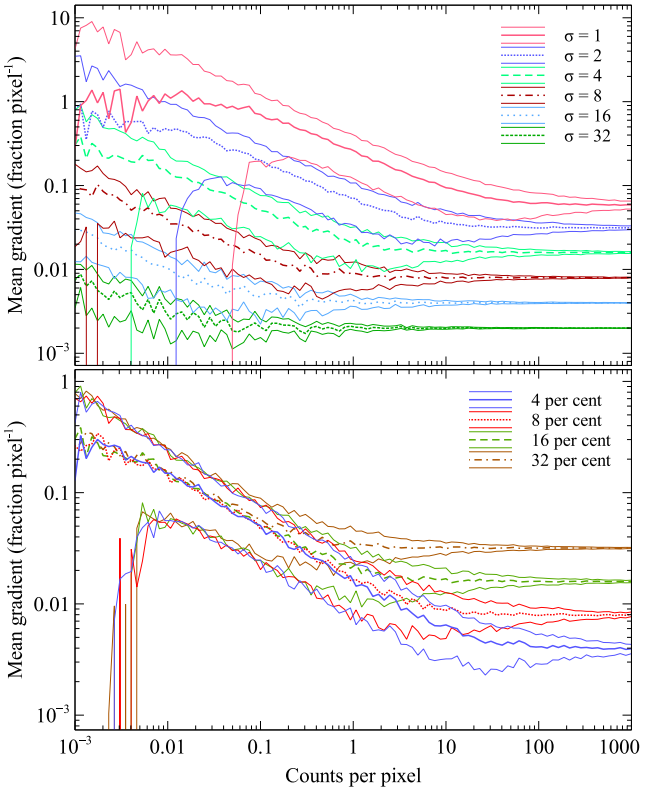

Figure 6. Fractional gradient value detected for a 1D sharp jump in surface brightness. The lines show the mean values and standard deviations as a function of surface brightness. (Top panel) Values using $\sigma = 1$, 2, 4, 8, 16 and 32 pixels for a 16 per cent jump. (Bottom panel) Values for jumps of 4, 8, 16 and 32 per cent using $\sigma = 4$ pixels.

over, the surface brightness and the value of σ. As the GGM filter computes a gradient magnitude, the output must always be zero or positive. Poisson fluctuations in the input image will therefore produce a noise signal in the output which is not removed by averaging over area.

To assess this quantitatively, we repeatedly filtered Poisson realizations of a simple model images with a 1D jump in surface brightness with zero width around a certain mean surface brightness. Fig. 6 (top panel) shows how the resulting gradient value at the jump pixel varies as a function of surface brightness and σ for a fixed fractional surface brightness jump. At low count rates, the gradient signal becomes increasingly dominated by noise. At higher count rates, the mean gradient tends towards a constant value and the standard deviation decreases. The noise signal at low count rates has the same Poisson error origin as the noise in the real signal at high count rates, scaling as the surface brightness to the power $-1/2$. This noise component also scales as $\sigma^{-1/2}$, as expected if sensitive to the number of counts within the filter. As the filter has a finite width and the jump is narrow, the determined gradient varies as $1/\sigma$. If a model with continuous gradient over a few σ is examined, its value is recovered for all values of σ.

The ability to detect a jump depends on the magnitude of the jump, shown using $\sigma = 4$ in Fig. 6 (lower panel). Jumps become more visible with increasing jump size and count rate. In this 1D case, the count rate at which the gradient diverges from the noise profile decreases with the inverse of the fractional magnitude of the jump.

3.3 Assessing the significance of structures

Although GGM filtering is a simple image analysis technique, it is important to assess the significance of features in resulting maps. Our ability to detect gradients depends on the count rate, size of gradient (in both magnitude and length) and σ (Section 3.2). The simplest method to assess significance is to compare the filtered image with raw data. Often structures can be directly observed in the raw data by using a colour scale well matched to the region in question, or by blinking between the filtered and original images. The significance of features can also be assessed by comparing them with the strength of noise at the same radius, where the count rate is likely to be similar. Filtered images can also be compared to unsharp-masked images or images with the radial average removed to ensure that features are robust. A further technique is to make a simulated cluster image, based on a smooth surface brightness profile or other model, and to filter this in the same way as the data. The real and simulated filtered images can then be compared to assess the significance of structures (see e.g. Figs 4 and 5). Comparison of images with those at other wavelengths can also confirm the existence of structures in filtered images (see Sections 3.4 and 3.7).

We examine a small region to the north-east of the Perseus cluster core (Fig. 7), showing a smoothed X-ray image, a GGM-filtered image, a filtered image of a simulation of the cluster with the same

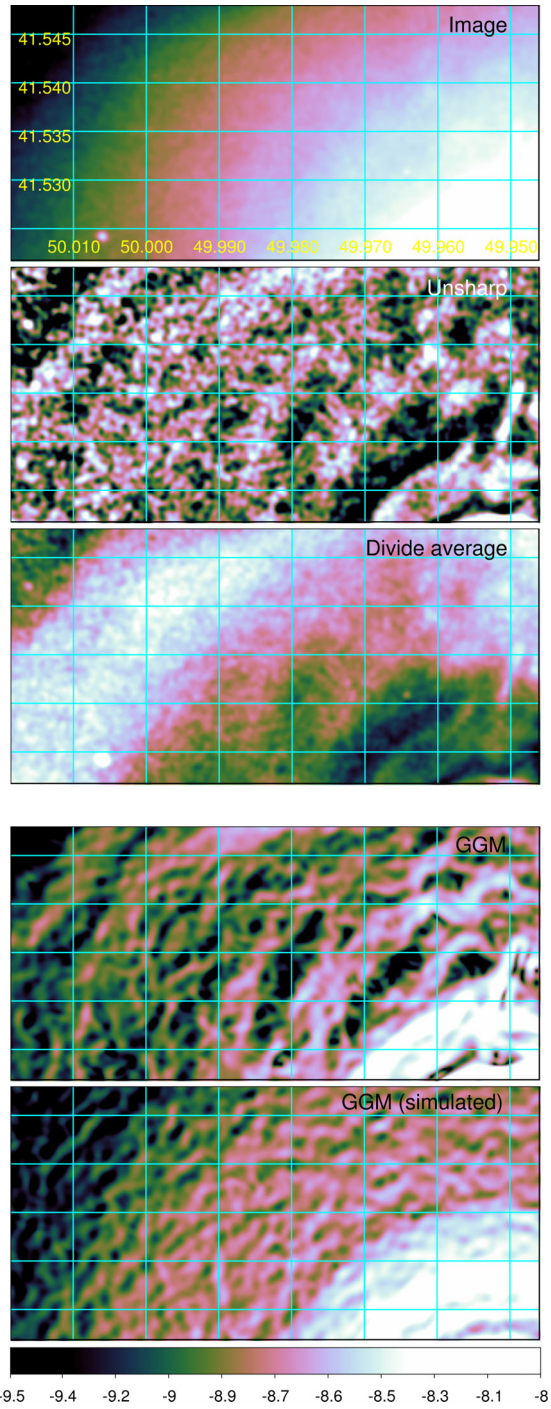

Figure 7. Comparison between different methods applied to the same region of Perseus. Top panel: X-ray image, smoothed by a $\sigma = 2$ Gaussian. Second panel: unsharp-masked image, dividing Gaussian-smoothed images with $\sigma = 2$ and 16 pixels. Third panel: ratio between data and average at each radius, smoothed using $\sigma = 2$. Fourth panel: GGM-filtered image ($\sigma = 4$, hiding point sources), with scale in $\log_{10}$ photon cm^{-2} s^{-1} pixel^{-1}, fifth panel: GGM-filtered simulated data with the average radial surface brightness as the real data and same colour scale as fourth panel.

radial profile, an unsharp-masked image and an image showing the fractional residuals to the average at each radius. The magnitude of the structures in the real data is much larger than those in the simulated filtered map, although we see that the real data has noise in it at a similar level to the filtered map. The noise patterns tend

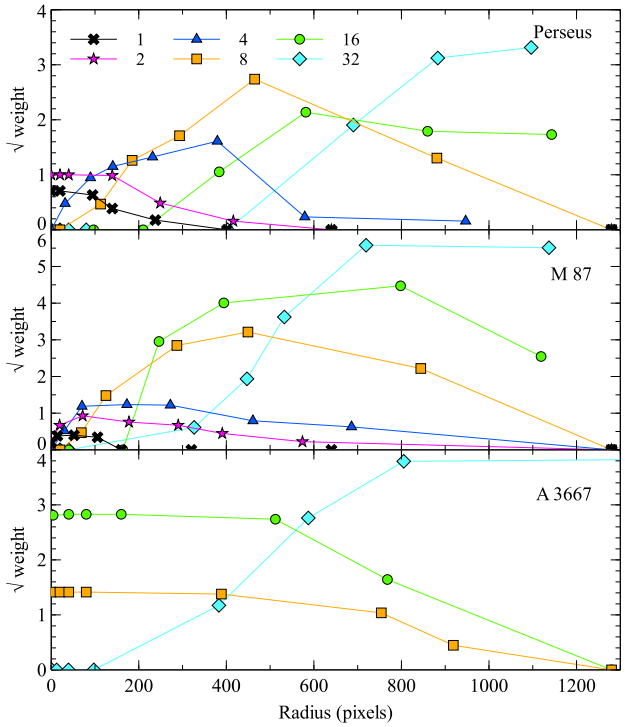

Figure 8. Radial profiles of the radial weights used when making the combined filtered images of the Perseus cluster, M 87 and A 3667.

to be small linear structures which lie perpendicular to the surface brightness gradient. The main gradient component that the filter is measuring is radial and so fluctuations due to noise are most strongly seen in the radial direction after filtering, leading to these characteristic noise patterns. A key method for assessing the level of noise is to look at the amount of noise in other directions, where the gradient and data quality are similar.

The A 3667 data (Fig. 4) highlight that the appearance of noise after the filtering process depends on the data quality. In the north-west parts of the 8 and 16 scale images, there are regions filled with fluctuating dark and bright structures. This is a region in the cluster which is only covered using relatively short exposures. Therefore, one must be careful when assessing features in filtered data where the data quality varies strongly over the image.

3.4 Combining images of different scales

Filtering on a certain length-scale is applicable to a particular region in the cluster, where the count rate is large enough to allow the gradient to be measured. We have therefore implemented a scheme where we add the images with different scales together, weighting each of the images using a radial weighting scheme. We adjust a number of control points (radius and weighting factor) and use linear interpolation to calculate the values for intermediate radii. The motivation for the radial weighting is that the number of counts, the main quantity which determines our ability to measure the gradient, mainly varies radially in clusters. The weighting procedure also allows the magnitude of the features in the centre to be suppressed relative to the outskirts, in order to plot them on the same image. We constructed a graphical user interface in order to adjust the different radial scaling factors. Fig. 8 shows the relative radial weights of the different filtered images for the three clusters.

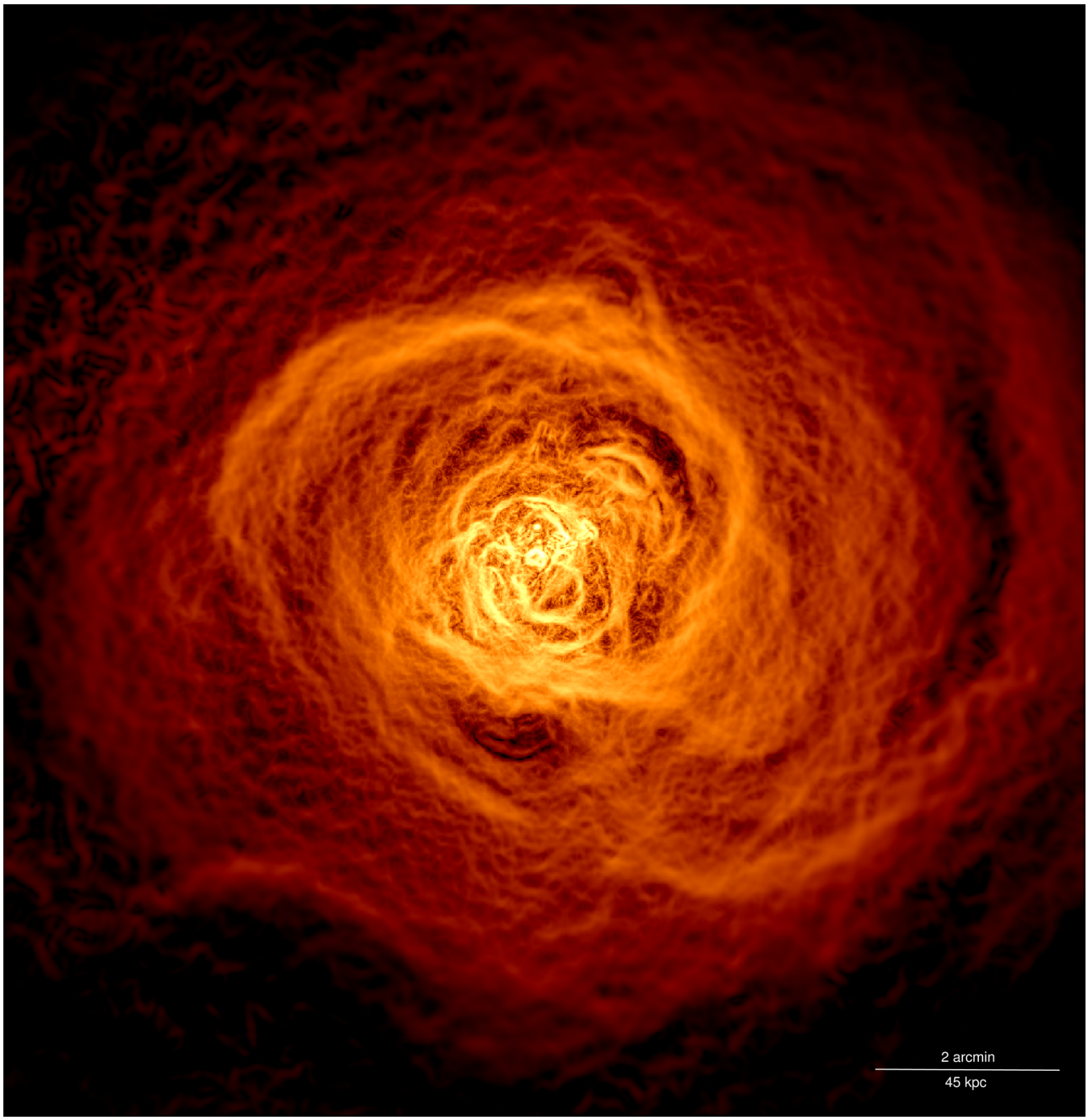

Figure 9. Combined GGM-filtered of the Perseus cluster, adding maps with $\sigma = 1$ to 32 pixels with radial weighting.

Fig. 9 shows the combined image for the Perseus cluster. In the inner part of the cluster, most of the signal comes from the $\sigma = 1$ and 2 maps, while in the outskirts the $\sigma = 8$, 16 and 32 maps are combined. Fig. 10 shows the combined results for M 87.

Fig. 11 compares the filtered X-rays with the 90 cm radio emission (Owen, Eilek & Kassim 2000), highlighting the close connection between the X-ray and radio-emitting plasmas. The radio source has two arms, one to the east with a 'mushroom' appearance and the other to the south-west with a filamentary structure. The south-western arm has a twisted appearance, where the X-rays and radio appear to be anticoincident, likely dominated by magnetic structures (Forman et al. 2007). The eastern arm, in contrast, has coincident X-ray and radio structures. This arm may be made up of a series of small radio bubbles plus the large radio torus which makes the cap of the mushroom (Forman et al. 2007). Much of the edge of large-scale radio structure is coincident with edges in the X-ray surface brightness.

Fig. 12 shows a map combining filtered images with scales of $\sigma = 8$, 16 and 32 pixels for A 3667. It highlights the sharp cold front edge and surface brightness plateau between the triangle structure and the central galaxy. The combined multiscale images demonstrate that it is possible to create useful qualitative maps which show the majority of the surface brightness edges in a galaxy cluster image.

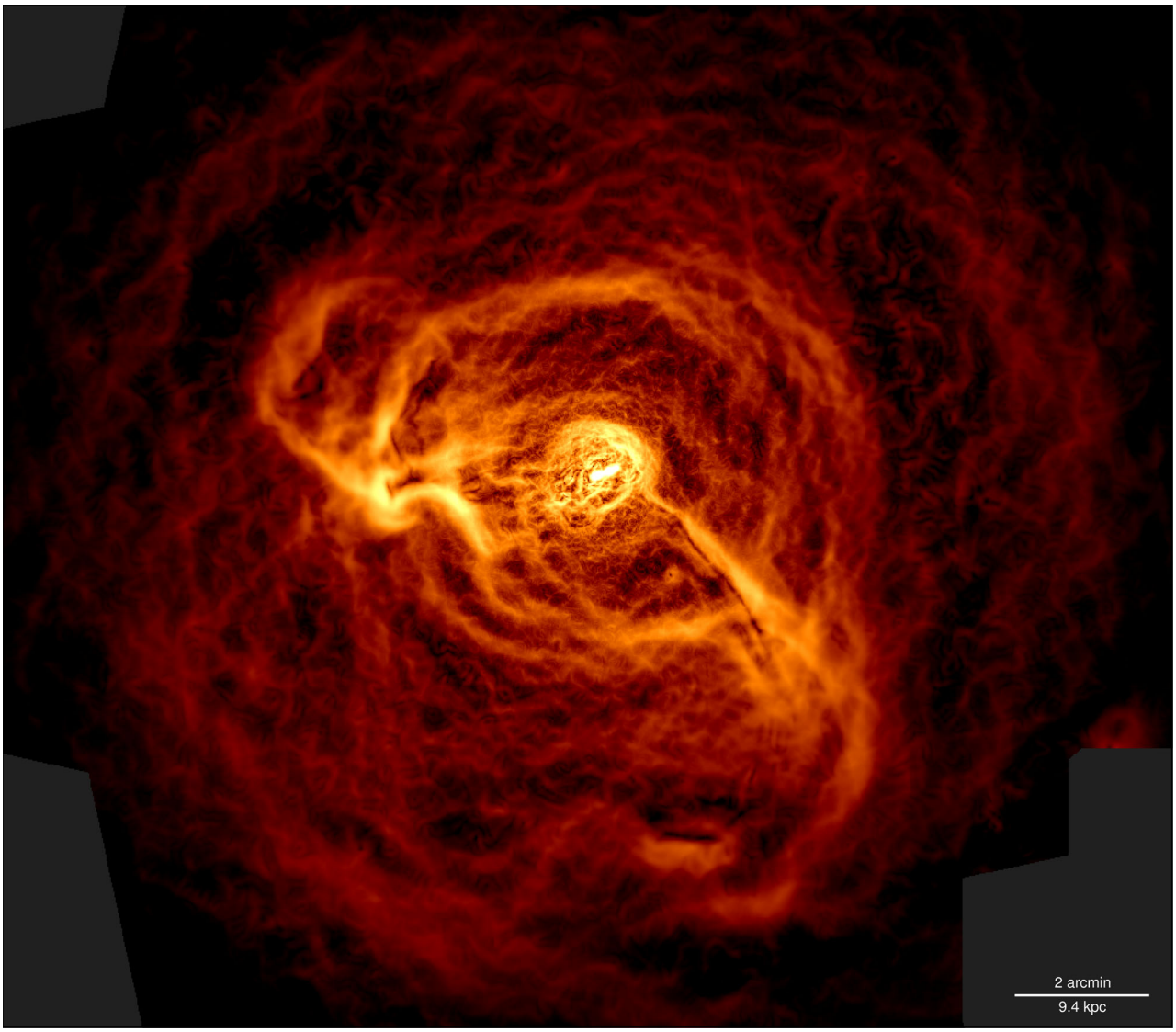

Figure 10. Combined GGM-filtered of M 87, adding maps with $\sigma = 1$ to 32 pixels with radial weighting.

3.5 Comparison with other methods

The GGM-filtered image of the example region (Fig. 7) clearly reveals the surface brightness edges in the data, particularly those associated with the ripple-like structures.

These ripples are not so easily seen in the image showing the fractional deviations from the radial average, likely due to them being mostly azimuthal in morphology. When subtracting models as here, the choice of a model can greatly influence the produced residual image (Sanders & Fabian 2012), so care must be taken to not introduce or remove important structures. It is difficult to construct models which replicate the complex structure seen, for example, as the spiral in the core of the Perseus cluster.

Unsharp masking does show the ripples here, but they have a relatively unclear and patchy appearance. This is similar to the results of an analysis of images of the Centaurus cluster, where the linear structures present are revealed using GGM filtering, but not using unsharp masking (Sanders et al. 2016). A disadvantage of gradient filtering over unsharp masking, however, is that intrinsically narrow filamentary structures are broadened, such as the filament to the north (on the western side of the image). A filament is converted to a double structure due to the sharp gradient on either side and the flat gradient along its ridge.

To compare unsharp masking and gradient filtering in more detail, we show in Fig. 13 the highly structured central region of M 87. Shown are the smoothed data, two unsharp-masked images (using different large and small smoothing scales) and three GGM-filtered images (using scales of 2, 4 and 8 pixels). Unsharp masking commonly produces negative artefacts surrounding bright sources (seen near the jet here), which are difficult to distinguish from, or mask, AGN-generated cavities in the ICM (labelled negative artefacts). Immediately surrounding the jet are filamentary structures (labelled inner filaments) visible in the GGM-filtered images which are lost in the unsharp-masked data, due to the large negative residual artefacts there.

Unsharp masking also produces similar negative artefacts at sharp surface brightness edges such as shocks or cold fronts, seen here to the north-west (labelled cold front (CF) edge). GGM-filtering does not produce similar signals which could otherwise be misinterpreted as cavities. The negative residuals around cold fronts in unsharp-masked images are an issue when trying to detect

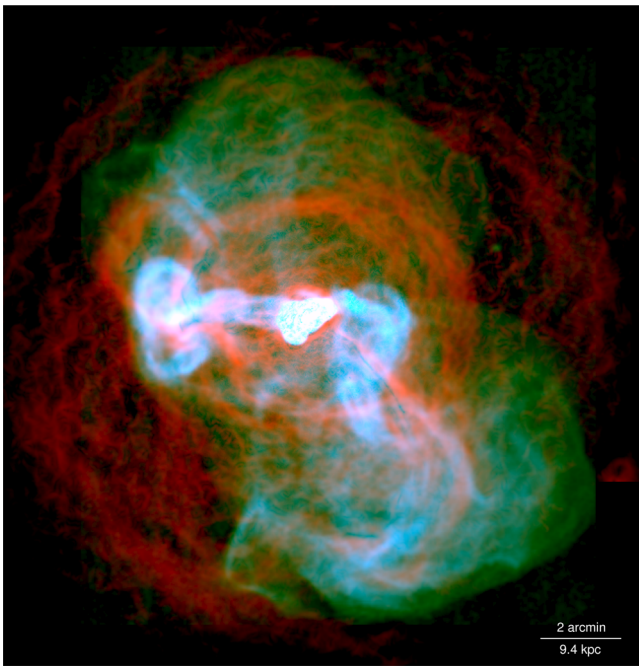

Figure 11. GGM-filtered X-ray image of M87 from Fig. 10 (red), overlaid with 90 cm radio emission from Owen et al. (2000) [blue/green].

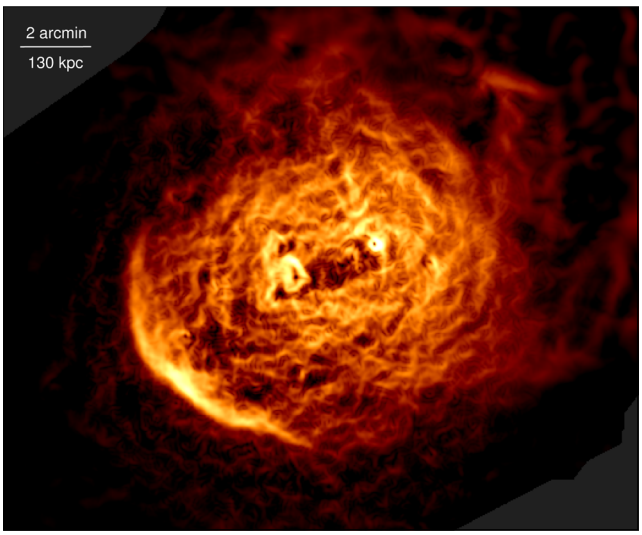

Figure 12. Combined GGM-filtered image of A 3667, adding maps with $\sigma = 8$, 16 and 32 with radial weighting.

cavities in more distant objects, where there can be large changes in surface brightness. Unsharp masking relies on a smoothed image being a good approximation for the underlying cluster emission, which is likely not to be the case in the peaked central regions. Some features are however clearer in the unsharp-masked images, particularly those which are smaller than the smoothing scale on a relatively flat background, for example the small depressions to the north of the image (labelled outer cavities). Nevertheless, the GGM-filtered $\sigma = 2$ and 4 images reveal a great deal of structure which is not obviously present in the unsharp-masked data. It is clear that continuous structures are better connected on this complex underlying cluster emission in the GGM-filtered images than when using unsharp masking.

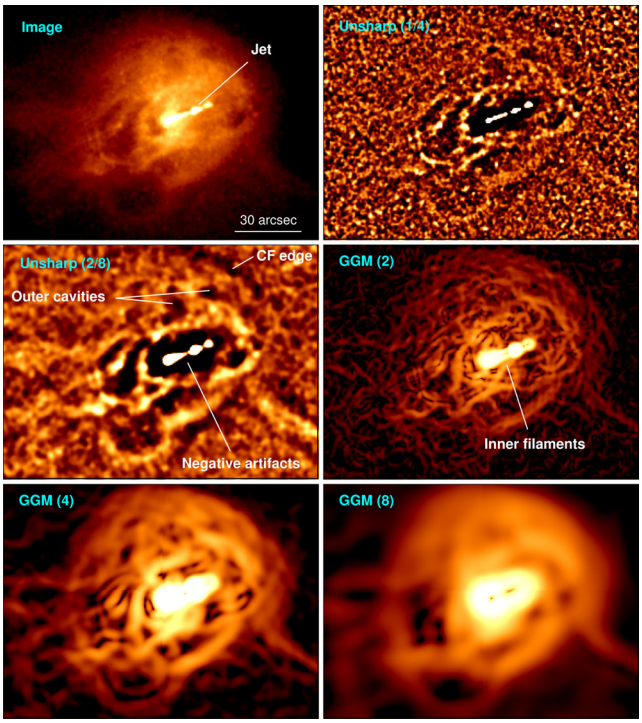

Figure 13. Comparison of unsharp masking and gradient filtering in the central region of M 87. Top-left panel: X-ray image with point sources removed and smoothed by a Gaussian of $\sigma = 1$ pixel. Top-right panel: unsharp masking, showing fractional difference between images smoothed by 1 and 4 pixels. Centre-left panel: unsharp masking using 2 and 8 pixels. Other panels: gradient filtered image with σ as value given in pixels.

Despite the power of the gradient filtering method, there are relative advantages and disadvantages of GGM filtering, unsharp masking and model subtraction. Therefore, a combination of the various techniques is likely to help reliably identify structures, particular at higher redshifts.

3.6 Logarithmic gradients

The average surface brightness profile for a galaxy cluster can be approximated by a power law in radius, at least over large radial regions. Ideally to identify where there are deviations from a smooth profile, it would be better to examine the gradient of the logarithm of the surface brightness in logarithmic radius, rather than in linear coordinates. We can partially achieve this by computing the logarithm of the surface brightness and applying a gradient filter to the resulting image. As X-ray images are noisy and there are often pixels with zero values, a better way of doing this is to first smooth the X-ray image with the Gaussian of the scale required, take the logarithm of the smoothed image, and then compute the pixel-by-pixel gradient magnitude.

This method can produce good results, as shown by the filtered image of Perseus in Fig. 14. The component of the gradient which comes from the cluster profile is significantly reduced. The image shows the structure from the inner shock out to the large-scale spiral using a single filtering scale.

A disadvantage of the technique is that the value becomes noisy where the count rate is low in the outskirts. When the gradient of a non-logarithmic X-ray image is computed, the pixels with low number of counts typically are in regions with low absolute

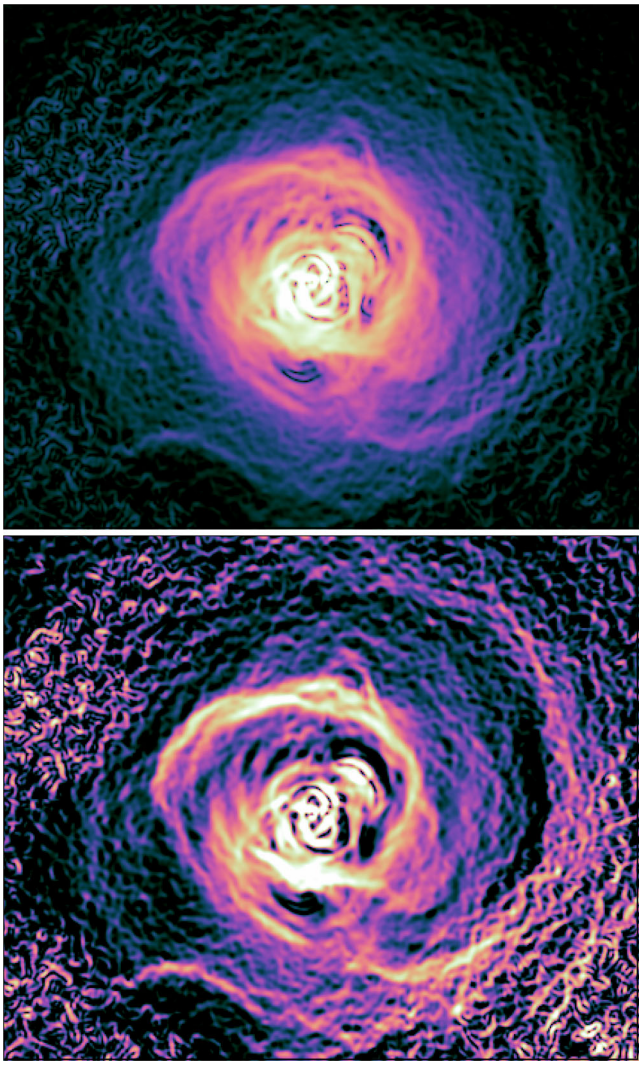

Figure 14. Gradient image of Perseus ($\sigma = 8$ pixels) [top panel] compared to a gradient of the log value of an image smoothed using a Gaussian of $\sigma = 8$ pixels (bottom panel).

gradients and so the noise on the gradient is low compared to the gradient value in the centre where the counts rate are high. However, using a logarithmic image, the gradient in the outskirts is similar to the value in the centre. As the count rate in the outskirts is lower, the scatter in the value is higher. This noise can be seen in the north-east and south-west parts of Fig. 14, where the observation is shallower and the cluster fainter.

Logarithmic gradient images are therefore likely preferred if there is a sufficiently high count rate across the region of interest so that the gradient can be measured to a high fractional accuracy. However, this criterion is unlikely to be met using typical photon-starved observations with *Chandra* except in the core region or using large spatial scales.

3.7 Finding shocks

As pointed out by Forman et al. (2007), between temperatures of around 1 and 3 keV the *Chandra* 3.5 to 7.5 keV band count rate is approximately proportional to the pressure-squared integrated along the line of sight. Therefore, by gradient filtering such images, we are able to detect pressure discontinuities and shocks in clusters.

Fig. 15 shows filtered images from scales of 4 to 32 pixels of M 87 in this hard X-ray band. In the centre is an egg-shaped region previously identified by Young et al. (2002), marked by A in the 4 and 8 scale maps. This is likely a high-pressure region created by the current AGN outburst. Surrounding this feature is a second edge in pressure (labelled B), seen clearly in the 8 map and at lower significance in the 4 map. At a radius of 13 kpc is the clearest shock (labelled C and D), believed to be driven by an earlier AGN episode approximately 14 Myr ago (Forman et al. 2007). Spectral fitting shows it to have a Mach number of 1.25 (Million et al. 2010).

The most interesting aspect of this image, in agreement with the full band image and filtered image, is that the 13-kpc shock is not a complete circle, but breaks up into multiple edges (C, D and E), with a further edge at lower surface brightness levels (F). Edges F and G are stronger than the noise at the same radius and can be seen in the unfiltered image. F lies at the edge of the south-west radio plume. The splitting up of the C, D and E structure may be due to varying temperature structure along the line of sight, affecting the sound speed. Alternatively, there could have been multiple outbursts.

In the Perseus cluster, the ICM is too hot for these hard-band images to be solely sensitive to pressure variations. However, in the central region around the inner cavities the 2.7 to 4 keV temperatures are close to the preferred range. Fig. 16 shows a filtered hard X-ray

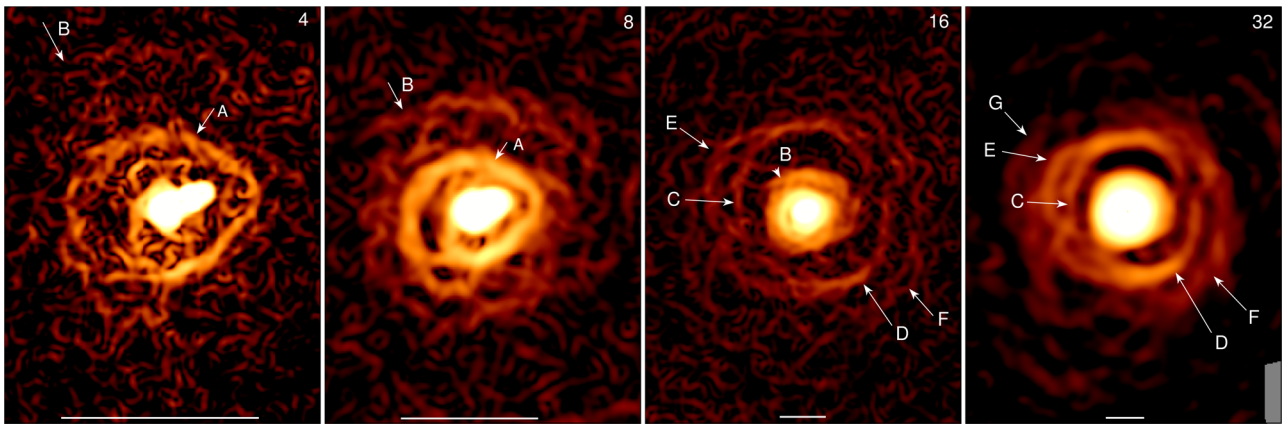

Figure 15. Pressure-jump-sensitive GGM-filtered hard-band 3.5 to 7.5 keV images of M 87. The images use $\sigma = 4$ to 32 pixels, showing a set of pressure discontinuities marked by arrows. The bar has a length of 1.5 arcmin (7.1 kpc).

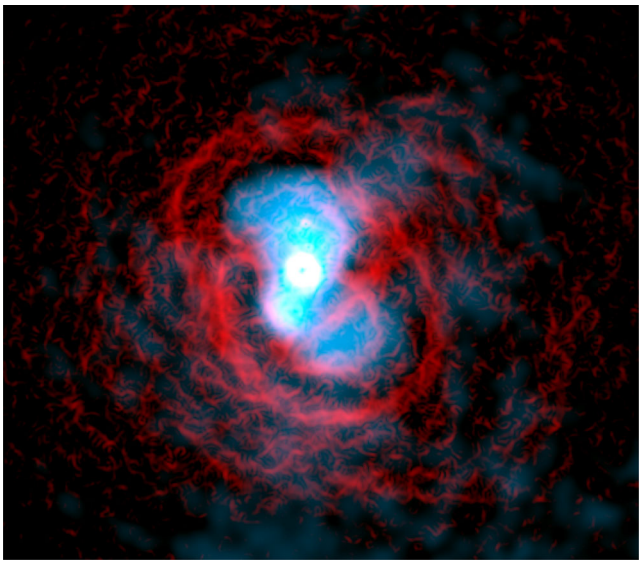

Figure 16. Filtered 3.5 to 7.5 keV X-ray image of Perseus (red) with 330 MHz radio emission (blue; Fabian et al. 2002). The X-ray image is a linear combination of the $\sigma = 2$, 4 and 8 pixels maps. The image measures 4.3 arcmin (96 kpc) across.

image of Perseus (combining three different scales), overlaying the radio emission. The image highlights the jumps in pressure at the edge of the shocks surrounding the inner cavities. The image can be interpreted as two shocks, one surrounding each bubble (as seen in a spectral fitting pressure map; Fabian et al. 2006). The southern rim of the northern shock appears to pass through the southern cavity and the rim of the northern rim of the southern shock appears to pass through the northern cavity. The straight feature across the southern cavity appears to be the edge of the shock and is not related directly to the radio source. To the north-west, the outer edge of the shock is much less clear, where the radio plasma extends from the northern inner cavity to the outer north-western ghost cavity.

4 CONCLUSIONS

We examine X-ray images of the Perseus cluster, M 87 and A 3667 with the GGM filter to detect edges. We show that the filter is able to detect a host of structures within these clusters. The method is often more sensitive to features than unsharp-masking or subtracting radial cluster models. It also does not introduce negative residual artefacts commonly seen in unsharp-masked images. By the use of a radial weighting scheme, we can produce a multiscale image which demonstrates that a wealth of physical processes are occurring in these clusters. Using pressure-sensitive hard-energy-band images it is possible to use the method to detect shocks in clusters.

SOFTWARE REPOSITORY

The code described and used in this paper can be found at https://github.com/jeremysanders/ggm.

ACKNOWLEDGEMENTS

ACF, HRR and SAW acknowledge support from the ERC Advanced Grant FEEDBACK. The scientific results reported in this article are based on data obtained from the *Chandra* Data Archive.

REFERENCES

Arnaud M. et al., 2001, A&A, 365, L67
Ascasibar Y., Markevitch M., 2006, ApJ, 650, 102
Blanton E. L., Randall S. W., Clarke T. E., Sarazin C. L., McNamara B. R., Douglass E. M., McDonald M., 2011, ApJ, 737, 99
Böhringer H., Voges W., Fabian A. C., Edge A. C., Neumann D. M., 1993, MNRAS, 264, L25
Böhringer H., Nulsen P. E. J., Braun R., Fabian A. C., 1995, MNRAS, 274, L67
Böhringer H., Matsushita K., Churazov E., Finoguenov A., Ikebe Y., 2004, A&A, 416, L21
Cappellari M. et al., 2011, MNRAS, 413, 813
Churazov E., Gilfanov M., Forman W., Jones C., 1999, ApJ, 520, 105
Churazov E., Forman W., Jones C., Böhringer H., 2003, ApJ, 590, 225
Churazov E. et al., 2012, MNRAS, 421, 1123
Fabian A. C., 2012, ARA&A, 50, 455
Fabian A. C. et al., 2000, MNRAS, 318, L65
Fabian A. C., Celotti A., Blundell K. M., Kassim N. E., Perley R. A., 2002, MNRAS, 331, 369
Fabian A. C., Sanders J. S., Allen S. W., Crawford C. S., Iwasawa K., Johnstone R. M., Schmidt R. W., Taylor G. B., 2003a, MNRAS, 344, L43
Fabian A. C., Sanders J. S., Crawford C. S., Conselice C. J., Gallagher J. S., Wyse R. F. G., 2003b, MNRAS, 344, L48
Fabian A. C., Sanders J. S., Taylor G. B., Allen S. W., Crawford C. S., Johnstone R. M., Iwasawa K., 2006, MNRAS, 366, 417
Fabian A. C. et al., 2011, MNRAS, 418, 2154
Felten J. E., Gould R. J., Stein W. A., Woolf N. J., 1966, ApJ, 146, 955
Finoguenov A., Sarazin C. L., Nakazawa K., Wik D. R., Clarke T. E., 2010, ApJ, 715, 1143
Forman W. et al., 2005, ApJ, 635, 894
Forman W. et al., 2007, ApJ, 665, 1057
Fruscione A. et al., 2006, in Silva D. R., Doxsey R. E., eds, Proc. SPIE Conf. Ser. Vol. 6270, Observatory Operations: Strategies, Processes, and Systems. SPIE, Bellingham, p. 1
Kalberla P. M. W., Burton W. B., Hartmann D., Arnal E. M., Bajaja E., Morras R., Pöppel W. G. L., 2005, A&A, 440, 775
Knopp G. P., Henry J. P., Briel U. G., 1996, ApJ, 472, 125
McNamara B. R. et al., 2000, ApJ, 534, L135
Markevitch M., Vikhlinin A., 2007, Phys. Rep., 443, 1
Markevitch M., Gonzalez A. H., David L., Vikhlinin A., Murray S., Forman W., Jones C., Tucker W., 2002, ApJ, 567, L27
Marshall H. L., Miller B. P., Davis D. S., Perlman E. S., Wise M., Canizares C. R., Harris D. E., 2002, ApJ, 564, 683
Mazzotta P., Fusco-Femiano R., Vikhlinin A., 2002, ApJ, 569, L31
Million E. T., Werner N., Simionescu A., Allen S. W., Nulsen P. E. J., Fabian A. C., Böhringer H., Sanders J. S., 2010, MNRAS, 407, 2046
Mitchell R. J., Culhane J. L., Davison P. J. N., Ives J. C., 1976, MNRAS, 175, 29P
Norman M. L., Bryan G. L., 1999, in Röser H.-J., Meisenheimer K., eds, Lecture Notes in Physics, Vol. 530, The Radio Galaxy Messier 87. Springer-Verlag, Berlin, p. 106
Owen F. N., Eilek J. A., Kassim N. E., 2000, ApJ, 543, 611
Paterno-Mahler R., Blanton E. L., Randall S. W., Clarke T. E., 2013, ApJ, 773, 114
Randall S. W. et al., 2015, ApJ, 805, 112
Roediger E., Kraft R. P., Forman W. R., Nulsen P. E. J., Churazov E., 2013, ApJ, 764, 60
Röttgering H. J. A., Wieringa M. H., Hunstead R. W., Ekers R. D., 1997, MNRAS, 290, 577
Russell H. R., Sanders J. S., Fabian A. C., Baum S. A., Donahue M., Edge A. C., McNamara B. R., O'Dea C. P., 2010, MNRAS, 406, 1721
Ruszkowski M., Brüggen M., Begelman M. C., 2004, ApJ, 611, 158
Sanders J. S., Fabian A. C., 2007, MNRAS, 381, 1381
Sanders J. S., Fabian A. C., 2008, MNRAS, 390, L93
Sanders J. S., Fabian A. C., 2012, MNRAS, 421, 726

Sanders J. S., Fabian A. C., Allen S. W., Schmidt R. W., 2004, MNRAS, 349, 952
Sanders J. S., Fabian A. C., Dunn R. J. H., 2005, MNRAS, 360, 133
Sanders J. S. et al., 2016, MNRAS, 457, 82
Sijacki D., Springel V., 2006, MNRAS, 366, 397
Simionescu A., Böhringer H., Brüggen M., Finoguenov A., 2007, A&A, 465, 749
Sodre L., Jr, Capelato H. V., Steiner J. E., Proust D., Mazure A., 1992, MNRAS, 259, 233
Struble M. F., Rood H. J., 1999, ApJS, 125, 35
Tonry J. L., Dressler A., Blakeslee J. P., Ajhar E. A., Fletcher A. B., Luppino G. A., Metzger M. R., Moore C. B., 2001, ApJ, 546, 681
Vikhlinin A., Markevitch M., Murray S. S., 2001, ApJ, 551, 160
Walker S. A., Sanders J. S., Fabian A. C., 2015, MNRAS, 453, 3699
Wilson A. S., Yang Y., 2002, ApJ, 568, 133
Young A. J., Wilson A. S., Mundell C. G., 2002, ApJ, 579, 560
Zhuravleva I. et al., 2014, ApJ, 788, L13

This paper has been typeset from a TEX/LATEX file prepared by the author.